In vivo two-photon voltage-sensitive dye imaging reveals top-down control of cortical layers 1 and 2 during wakefulness

B. Kuhn*†‡, W. Denk*‡, and R. M. Bruno*‡§

*Max Planck Institute for Medical Research, Jahnstrasse 29, 69120 Heidelberg, Germany; and †Lewis Thomas Laboratory, Princeton University, Princeton, NJ 08544

Conventional methods of imaging membrane potential changes have limited spatial resolution, particularly along the axis perpendicular to the cortical surface. The laminar organization of the cortex suggests, however, that the distribution of activity in depth is not uniform. We developed a technique to resolve network activity of different cortical layers *in vivo* using two-photon microscopy of the voltage-sensitive dye (VSD) ANNINE-6. We imaged spontaneous voltage changes in the barrel field of the somatosensory cortex of head-restrained mice and analyzed their spatio-temporal correlations during anesthesia and wakefulness. EEG recordings always correlated more strongly with VSD signals in layer (L) 2 than in L1. Nearby (<200 μm) cortical areas were correlated with one another during anesthesia. Waking the mouse strongly desynchronized neighboring cortical areas in L1 in the 4- to 10-Hz frequency band. Wakefulness also slightly increased synchrony of neighboring territories in L2 in the 0.5- to 4.0-Hz range. Our observations are consistent with the idea that, in the awake animal, long-range inputs to L1 of the sensory cortex from various cortical and thalamic areas exert top-down control on sensory processing.

anesthesia | apical dendrite | awake | axon | synchrony

Layer (L) 1 has been least investigated of all the cortical layers despite its potentially prominent role in cortical processing. Although largely acellular, except for a sparse population of inhibitory neurons (1), L1 is the main target of axons originating in distant cortical and subcortical regions. This dense plexus of axons makes excitatory synapses on apical dendritic tufts of L2/3 and L5 pyramidal neurons. Dendritic tufts contain powerful active conductances that cause electrical changes that can propagate to their relatively distant somata and influence the integration of synaptic inputs there (2). L1 is therefore ideally positioned to mediate communication between brain regions.

In the primary somatosensory cortex, long-range input to L1 consists of corticocortical synapses from primary motor cortex and the secondary somatosensory area (3). In contrast, synapses in other cortical layers, such as L2, originate from a mixture of excitatory and inhibitory cells located mainly in that specific cortical column (4). A major source of thalamocortical synapses in L1 is the second-order sensory nucleus, also called the "posterior medial" (POm) nucleus (5), whose activity appears to be strongly modulated by arousal (6). This finding suggests that synaptic inputs in L1 also should be modulated by arousal. Synaptic inputs can be studied by recording membrane-voltage (V_m) changes, but L1 is relatively inaccessible using conventional methods.

Wide-field imaging of voltage-sensitive dyes (VSDs) has been used successfully to sample V_m in neurites of isolated neurons and across large populations of cortical cells (7). Although such imaging allows high frame rates (>1 kHz), scattering and limited depth discrimination result in poor spatial resolution. Thus, when imaging *in vivo*, the signal at any point in the image contains V_m information averaged laterally and in depth over as much as several hundred micrometers. Such spatial resolution might be surpassed even by current-source density (CSD) analysis (8), a very different electrode-based technique that compares local field potentials recorded simultaneously at different depths. However, to achieve resolution in the horizontal plane, CSD requires the invasive insertion of large electrode arrays.

Intracellular recording can monitor V_m *in vivo* with submillisecond resolution from various compartments, including somata (9, 10), apical tufts (11, 12), and basal dendrites (13), and it can even be used to measure individual synapse strengths (14). A pipette can, however, access only one compartment, limiting analysis at the network level. Indeed, multiple intracellular recordings *in vivo* are extremely difficult (15).

We therefore developed an approach to resolve network activity *in vivo* in individual layers that is based on two-photon fluorescence microscopy (16) of the VSD ANNINE-6 (17, 18), which allows two-photon excitation at the long-wavelength edge of the spectrum where the dye is most voltage-sensitive (19). We imaged spontaneous and sensory-evoked V_m changes in the barrel cortex of head-restrained mice and analyzed their spatio-temporal correlations during anesthesia and wakefulness to examine the differential effect of arousal on L1 and L2.

Results

Depth-Resolved VSD Recording. We imaged the barrel cortex of anesthetized mice through a skull surgically thinned to transparency (Fig. 1a). Regions corresponding to a few large facial whiskers were identified by imaging intrinsic reflectivity changes under ketamine/xylazine anesthesia (Fig. 1b). This area was then stained with VSD that was pressure-ejected at a depth of 100–200 μm. The light path was switched over to the two-photon microscope, and line scans (Fig. 1a, white line) were recorded through the center of a barrel column at various depths down to 400 μm. Whisker deflection triggered a decrease in fluorescence (negative $\Delta F/F$) at all depths (for an example, see Fig. 1c). A decrease was expected because depolarization shifts (18) the ANNINE-6 spectrum to shorter wavelengths (assuming that mainly the outer membrane leaflet is stained), which decreases signal for long-edge excitation (19).

Evoked responses became more pronounced with depth (Fig. 1d), indicating larger depolarizations and/or a higher proportion of active membrane at deeper imaging sites. The response in the column center increased from $-0.31\% \pm 0.10\%$ (mean $\pm$ SEM,

Fig. 1. VSD responses to sensory stimulation can be imaged by two-photon microscopy. (*a*) Combined *in vivo* setup for intrinsic and two-photon imaging. (*b*) Superposition of a reflected-light image of the surface vasculature and barrel positions (blue, C1; magenta, C2; green, C3). Colored areas show where reflectivity changes were >0.1% in response to whisker deflection. White line, line scan position and length during two-photon imaging. (*c*) Averaged (*n* = 400 trials) dye responses to whisker stimulation for focal depths of 40, 200, and 400 μm at an excitation wavelength of 1,020 nm. Dashed line, onset of stimulation of C2, the principal whisker for the line scan position. Red, fits of α function. (*d–f*) VSD signal amplitude in units of Δ*F/F* (*d*), latency (*e*), and decay (*f*) as a function of depth (*n* = 4 mice). (*g*) VSD signal for 960- and 1,020-nm excitation at a depth of 80 μm under identical stimulus conditions (200 trials).

fractional change; *n* = 4 mice) at a depth of 40 μm to −0.79% ± 0.10% at 160 μm and stays relatively constant down to 400 μm. The adjacent columns responded to stimulation of the same whisker with −0.28% ± 0.10% and −0.66% ± 0.09%, respectively. Mechanical deflection of one whisker and airpuff stimulation of the entire mystacial pad evoked up to −1.2% and −2.0% changes, respectively. Such changes are four times larger than those seen in the same preparation with wide-field imaging of RH-series dyes (20). These signals are, however, still small compared with Ca^{2+} indicator signals *in vivo* (21) even when bulk loaded (22). To attain a sufficient signal-to-noise ratio, some form of averaging of VSD signals is needed in time and/or space.

Latencies of sensory-evoked signals (see *Methods*) were ≈12 ms and largely depth-independent (Fig. 1*e*), except at a depth of 40 μm, where latency was more than doubled. The decay time constant (≈60 ms) increased slightly with depth (Fig. 1*f*). The time courses of these signals are in good agreement with wide-field VSD recordings, which appear to represent mainly L2/3 postsynaptic potentials (23, 24), as well as with intracellular recordings of neurons in L1 and L2/3 (12, 25).

To confirm that the signals we observe reflect V_m changes, we exploited the fact that absorbance changes due to the Stark effect are strongly excitation wavelength-dependent, as shown for ANNINE-6 using both one-photon (18) and two-photon (19)

excitation. At the same spatial location and for deflection of the same principal whisker, fractional fluorescence changes were −0.28% at 960 nm and −0.45% at 1,020 nm (Fig. 1*g*). The ratio between those values (1.6) closely matches that expected from *in vitro* data (19). Because action potentials only briefly depolarize the membrane and often are followed by a hyperpolarization, making the average voltage change rather small (26), they should not contribute much to the signals recorded here. Thus, two-photon imaging of ANNINE-6 can be used to monitor cortical V_m changes *in vivo*.

Spontaneous Activity in Anesthetized and Awake States. We studied the effect of arousal by examining spontaneous activity in L1 and L2 of mice under awake and anesthetized conditions. Two-photon line scans (Fig. 2*a*) at 40, 80, 120, or 160 μm below the pia, where dye staining is homogenous [supporting information (SI) Fig. S1], and the EEG (Fig. 2*b*) were recorded from isoflurane-anesthetized mice. Measurements at 40 and 80 μm are in L1, where images show blood vessels, but few cell bodies, whereas those at 120 and 160 μm are in L2, where numerous cell bodies are apparent as dark patches ≈8 μm in diameter (Fig. 2*a*). After imaging under anesthesia, the anesthetic gas was switched off. Several minutes later, sleep spindles disappeared from the EEG (Fig. 2*b*), and the mouse made whisker and paw movements, indicating that the mouse was now awake (27). Imaging was then repeated. Afterward, the gas was restored; when sleep spindles reappeared, the area was reimaged. This sequence was performed at all four depths.

At the full temporal resolution (2 ms) and with spatial averaging along a quarter of the line scan length (Fig. 2*a*, orange segment), the signals are still dominated by noise (Fig. 2*b*, orange trace). When averaging for 200 ms in time and along the whole line scan, fluorescence transients emerge that correspond to EEG activity (black traces).

Due to the limited signal-to-noise ratio, most spontaneous events are not directly visible. Event averaging (e.g., to a stimulus) is not possible for spontaneous activity, and temporal/spatial averaging might eliminate the very information desired. Therefore, we used more sophisticated statistical tools to analyze spontaneous activity. Cross-correlations (CCs) between the EEG and unfiltered VSD signal (Fig. 2*c*), as well as between pairs of line scan segments of the unfiltered VSD signal (Fig. 2*d*), show substantial structure.

CC of EEG and VSD Fluorescence. The CC of EEG and VSD signal always shows a peak ≈200 ms wide at Δ*t* = 0 s (*n* = 9 mice) (Fig. 2*e*). In the awake state, this correlation between the EEG (a weighted average of global current sinks and sources) and the VSD signal (local V_m) increases with depth (compare red traces in Fig. 2*e*). This finding suggests that the main component of the awake EEG originates from deeper layers. The small CC between EEG and L1 VSD signal during wakefulness (Fig. 2*e Left*) could be due to overall lower or less-synchronized neuronal activity.

Another prominent change in the CC occurs at negative time shifts (EEG preceding VSD signal), where EEG and VSD signal are anticorrelated. The anticorrelation extends up to about −1.8 s and is much stronger and increases with depth under anesthesia (blue). In awake mice, the effect reaches to only −0.8 s and almost vanishes at depths of 40 and 80 μm (red). At the larger depths, the signals are inversely correlated, although they are reduced in size and shifted toward shorter times. This anticorrelation is likely due to the different time courses of the local V_m changes measured by the dye and the EEG, the derivative of net V_m changes occurring across the brain.

Correlations Between Neighboring Regions. The synchrony of neighboring cortical areas was assessed by cross-correlating their
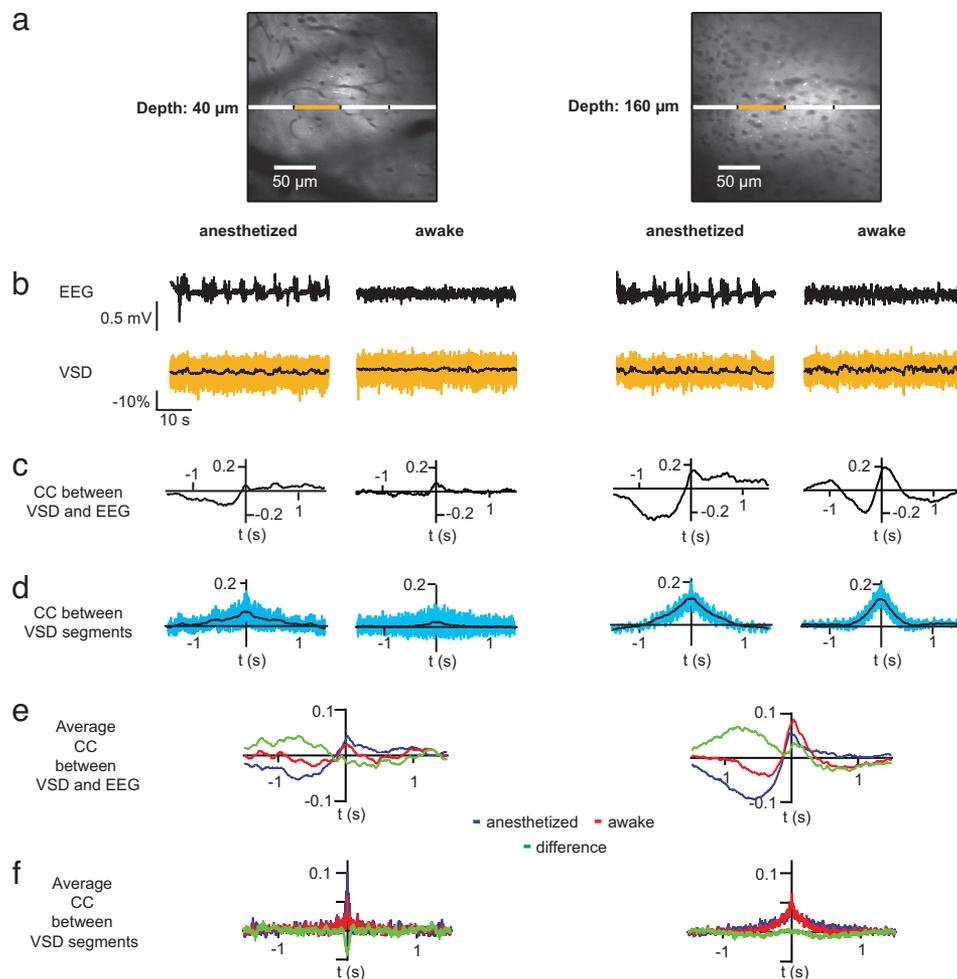
NEUROSCIENCE

Fig. 2. Imaging and time-domain correlation analysis of spontaneous activity. (*a*) Two-photon images at depths of 40 μm (*Left*) and 160 μm (*Right*) below the pia. Lines across image centers, line scan segments used for calculation of CC and coherence. (*b–d*) Data from one animal. (*e* and *f*) Pooled data (*n* = 9 mice). (*b*) EEG (*Upper*) and simultaneously measured VSD signals (*Lower*) show corresponding activity. Orange trace, average over the pixels of the orange segment in *a*; black trace, 200-ms boxcar filtered. (*c*) CC of total VSD signal and EEG. (*d*) CC of adjacent 64-μm-wide segments of the VSD signals averaged over all pairs. (*e* and *f*) Same as in *c* and *d*, except pooled over all mice.

spontaneous activity. The average CC of all possible pairings of adjacent 64-μm-wide line scan segments always peaked at $\Delta t = 0$ s (Fig. 2*f*). Under anesthesia, peak amplitude decreased from 0.125 at a depth of 40 μm to 0.085 at 160 μm (blue); in the awake state, it decreased from 0.095 to 0.075 (red). The difference between anesthetized and awake CCs (green) is largest at 40 μm and decreases monotonically with depth. At 160 μm, the difference is close to zero. With depth, CCs during both anesthesia and wakefulness also widen significantly from 45 $\pm$ 20 ms (FWHM) at 40 μm to 145 $\pm$ 71 ms at 160 μm ($P < 0.005$).

The fluctuations and their correlations also were analyzed in the frequency domain [pooled data (Fig. 3) and single experiment (Fig. S2)] by using power spectra (PS) and coherence, an intrinsically normalized (ranging from 0–1) measure of correlation, which are better suited for averaging across animals (28). The average EEG power spectra during imaging at the most superficial and deep locations have similar spectral content and are similarly reduced by waking (Fig. 3*a*, compare *Left* and *Right*), confirming that the mice were in comparable states when examined at different depths. Waking the mice decreases slightly the average PS of the VSD signals at 40 μm and increases it at 160 μm (Fig. 3*b*). The average coherence of the EEG and VSD is stronger for deeper depths (Fig. 3*c*),

which is consistent with the CCs and another indication of a deep layer origin of the EEG.

Spatial Correlations over Distance. The average coherence between neighboring cortical regions is notably increased at a depth of 160 μm when the mouse wakes up (Fig. 3*d Right*); this change is largely confined to frequencies <4 Hz. Note, however, that the average coherence is decreased by wakefulness at frequencies >4 Hz at 40 μm, an effect easily overlooked due to the small absolute values in this range (Fig. 3*d Left*). Coherence values were therefore summed within two frequency bands: 0.5–4 Hz and 4–10 Hz. Wakefulness decreased the high-frequency coherence of neighboring cortical regions in L1, but increased the low-frequeny coherence in L2 (Fig. 3*e*).

The distance dependence of correlation within a layer was analyzed at higher spatial resolution. Coherence was calculated between all possible combinations of shorter (16-μm-long) segments. Mean coherence decreased with distance at all depths, under both anesthetized and awake conditions, and in both frequency bands (Fig. 3*f*).

To compare the degree of spatial correlation for different conditions, we calculated the ratio between awake and anesthetized curves. In the awake state, L1 coherence was significantly smaller in the higher frequency band (coherence ratios: 0.5–4.0
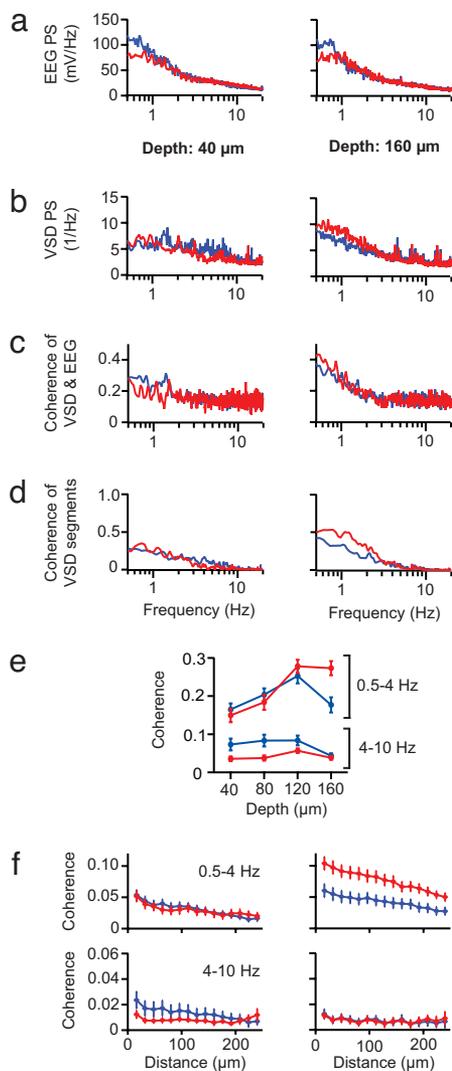
Fig. 3. Frequency domain analysis. Average (*n* = 9) power and coherence spectra (magnitude) of EEG and VSD for two depths (L1, 40 μm; L2, 160 μm) and for different arousal states. (*a* and *b*) Power spectra of the EEG (*a*) and VSD (*b*) for anesthetized (blue) and awake (red) states. (*c* and *d*) Coherence was either between the EEG and the VSD signal for the entire line scan length (*c*) or between adjacent 64-μm-wide line segments (*d*). Power and coherence spectra were smoothed with a 0.25-Hz boxcar. (*e*) Coherence within specific bands (either 0.5–4 Hz or 4–10 Hz) as a function of depth. (*f*) Coherence as a function of distance.

Hz, 0.92 ± 0.12, paired *t* test, *P* = 0.47; 4.0–10.0 Hz, 0.53 ± 0.13, *P* < 0.001). Coherence was, however, larger in L2 compared with the anesthetized state for lower frequencies (0.5–4.0 Hz, 1.50 ± 0.09, *P* < 0.05; 4.0–10.0 Hz, 0.78 ± 0.15, *P* < 0.05) (Fig. 3 *e* and *f*). The distance dependence of the spatial coherence was not affected by arousal (Fig. 3*f*). Averaging the ratios spanning separations of 16–200 μm results in a coherence ratio of 1.13 ± 0.07 for L2 (depth 120–160 μm) and 0.60 ± 0.10 for L1 (depth 40–80 μm) (Fig. 4, black), indicating a slight increase of L2 synchrony, but a marked decrease of L1 synchrony. In contrast, the ratios of power spectra calculated over the same frequency bands in L1 (0.5–4.0 Hz, 0.92 ± 0.11; 4.0–10.0 Hz, 0.94 ± 0.09) and L2 (0.5–4.0 Hz, 0.93 ± 0.11; 4.0–10.0 Hz, 0.95 ± 0.10) are quite constant. This result means that the changes in coherence during wakefulness cannot be explained by a change in spectral power.
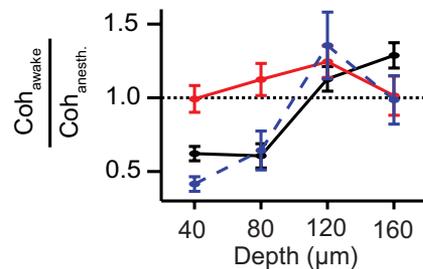
Fig. 4. AMPA/kainate receptors are required for coherence to be state-dependent. Ratio of coherence during wakefulness to coherence during anesthesia before CNQX (black), during CNQX (red), and after washout (blue) (*n* = 3).

Correlation Depends on Excitatory Transmission. As an additional control that the observed state-dependent synchrony is a neural phenomenon, we blocked excitatory synaptic inputs. Topical application of an AMPA/kainate receptor antagonist (6-cyano-7-nitroquinoxaline-2,3-dione, CNQX) to the cortical surface (*n* = 3 mice) had two effects. First, although CNQX did not change the PS (data not shown), it did reduce spatial coherence in anesthetized and wakeful mice at all depths compared with control conditions. Second, the differences between anesthetized and awake states were abolished; with CNQX the coherence ratios were 1.06 ± 0.14 in L1 and 1.12 ± 0.16 in L2 (Fig. 4, red). Washing out CNQX restored predrug behavior (Fig. 4, blue). The awake/anesthetized power-spectral ratio did not change significantly (with CNQX: L1 1.00 ± 0.18, L2 1.00 ± 0.14; control: 0.97 ± 0.10, 1.00 ± 0.10, respectively).

Discussion

We have demonstrated that two-photon imaging of VSD fluorescence makes possible depth-resolved optical voltage recordings with high temporal and spatial resolution in anesthetized and awake animals.

Expected Size of the VSD Signal *in Vivo*. Bulk loading VSD into the cortex stains the outer membranes of all cells. Because glia do not exhibit V_m changes to the same extent as neurons and because axonal signals are brief and bipolar, the observed changes in fluorescence are mainly generated by neuronal dendrites (23, 26, 29). Thus, axonal and glial membranes contribute mainly to background fluorescence, which increases photon shot noise and reduces fractional changes. By comparing the surface areas of dendrites, axons, and glia, we can estimate the signal size expected due to typical dendritic V_m fluctuations. Dendrites (including spines), axons (including boutons), and glia have surface areas of ≈15 cm², 46 cm², and 3.7 cm² per mm³ cortex, respectively (estimates based on refs. 30 and 31). Dendrites thus contribute 23% to the total surface area, and the expected V_m signal would be only 23% of the signal expected if dendrites alone were stained. An overall fluctuation of 10 mV and a dye sensitivity (19) of −0.49% per mV at 1,020-nm excitation should thus result in a −1.1% change in fluorescence. The signals we measured were typically in the range of 0.5–2%, which would correspond to mean dendritic depolarizations of ≈4–18 mV.

Layer-Specific Synchrony Changes. Because many of their calibers are well below the wavelength of light, neuronal processes in unspecifically stained, dense neuropil are generally not resolvable. Therefore, we cannot measure voltage in individual neurites. We can, however, test how V_m fluctuations in nearby locations relate to each other. Activity (assessed by PS) and synchrony (assessed by coherence) occur primarily at <10 Hz,

which is consistent with the typical spectra of ongoing synaptic input (32).

How do voltage fluctuations in different parts of cortex become correlated? Within a dendrite, voltage fluctuations become correlated as local voltage changes caused by synaptic input spread electrotonically or trigger dendritic spikes. This would happen even if the synaptic inputs were completely uncorrelated, which is unlikely. Correlations between synaptic inputs can occur even if axons fire independently because all boutons of an axonal arbor are activated by each spike. However, because each axon typically makes few contacts with any one dendrite, this mechanism does not lead to additional within-dendrite correlation, but does synchronize different dendrites. Finally, the synchrony of different axons can further correlate neighboring cortical areas.

Why does correlated activity decrease upon waking in L1 but increase in L2? L1 is unique, containing a dense plexus of axons arising from distant regions, namely primary motor cortex, secondary somatosensory cortex, and the POm thalamic nucleus (3, 33). CSD analysis of evoked surface potential recordings in primate somatosensory cortex first suggested that these long-range inputs are inactive during slow-wave sleep and anesthesia (34, 35). Indeed, intracellular recording showed that primate motor cortex neurons are tonically more depolarized during wakefulness (10), and work in rodents has shown that arousal strongly modulates POm activity via intrathalamic inhibition (6). Further evidence along these lines is that activity in S2 can modulate surface-evoked potentials in S1 of awake animals (36). Our data are consistent with the idea that wakefulness activates long-range inputs to sensory cortex. Local connections lead to correlated dendritic activity, which is then desynchronized by excitatory input to L1 as the animal wakes up. Although L1 is subject to arousal-dependent cholinergic modulation (33, 37, 38), the fact that blocking AMPA/kainate receptors removes state-dependent synchrony argues against acetylcholine as a mechanism.

How likely is it that modulation of electrotonic spread in dendritic tufts contribute to the arousal-state dependence of local correlations? Active conductances, which are engaged by strong input, can profoundly change voltage-spreading properties: A dendritic spike can quickly spread excitation throughout a dendrite, but electrogenic events also can be confined to individual branches (39). Even without engaging active currents, synaptic conductances will modulate the electrotonic length constant. Furthermore, as regenerative events propagate forward along the apical trunk into the soma and basal dendrites, they will increase synchrony in L2. Deeper compartments also may be more strongly influenced by dendritic spikes in the tufts than by the underlying distal synaptic inputs. State-dependent changes in L2 may appear in the lower frequency band because forward-propagating dendritic spikes can have lower frequency content than their underlying distal inputs.

Our measurements add weight to the idea that long-range L1 inputs exert top-down control over the processing of afferent information (34) in sensory areas. Awake-animal two-photon Ca^{2+} or V_m imaging might tell whether this is, for example, due to long-lasting opening of NMDA-mediated conductances in the apical tuft, in turn facilitating dendritic Ca^{2+} spike generation and biasing the neuron toward discharging during afferent input (2). Such a mechanism could underlie attentional focusing (40) and/or "event holding" (41).

Our results suggest that apical-tuft processes are more independent during the awake state. They may be even more so during active behavior. Imaging VSD-filled pyramidal neurons (reviewed in ref. 42) may be able to determine to what extent voltage asynchrony exists within individual apical tufts.

Methods

Surgery. All procedures were performed in accordance with the Max–Planck–Society's animal welfare guidelines. Briefly, 4- to 5-week-old C57/Black6 mice were anesthetized with 80/12 mg/ml ketamine/xylazine (1 μl/g of body weight; Sigma). The skull over barrel cortex was thinned to ≈50-μm thickness so that a ≈1.5 × 1.5-mm² region, centered 1.5 mm posterior of bregma and 3 mm lateral of the midline, was transparent when wet. A small hole was made in the thinned bone, leaving the dura intact. For CNQX experiments, the bone was removed over a 0.5 × 0.5-mm² area. To record the EEG, two silver wires were inserted under the skin ≈1.5 mm posterior and anterior, respectively, to the injection site. The skull was coated with superglue, and a dental-acrylic well was constructed. To immobilize the head, a post was attached to the skull by acrylic. ANNINE-6 was dissolved to saturation (≈0.5 mM) in DMSO with 20% Pluronic and then diluted 1:50 in 0.9% NaCl, of which ≈0.5 μl was injected over ≈15 min into the cortex at a depth of 100–200 μm with a quartz pipette (5- to 10-μm opening), which can penetrate dura. The well was filled with 1.5% agarose in 0.9% NaCl and coverslipped. The mouse was given 8 h to recover to avoid any effects of DMSO and, for measurements under isoflurane, ketamine/xylazine on imaging and to allow the dye to spread evenly. Postmortem histology of fixed tissue revealed no damage due to injection.

Imaging. The imaging setup allowed two-photon and reflected-light imaging alternately but of the same field of view. To image intrinsic signals, the thinned skull was obliquely illuminated with filtered (630 ± 15 nm) light from a power-stabilized halogen lamp. A single whisker was deflected by a piezo three times for 100 ms with 100-ms pauses. Fifty movies (3,000 frames each) were recorded at 500 Hz (NeuroCCD-SM; Redshirt Imaging) by using a 4×/0.1 NA objective (Zeiss) and averaged. The interstimulus interval was 30 s. An image was taken under 510 ± 10-nm illumination to record the blood vessel pattern. The sensory-evoked map of the barrel positions superimposed on the vasculature image was used to target dye injection and VSD imaging.

For two-photon imaging, the excitation wavelength was in the range of 1,020 nm (except for Fig. 1g), and the objective was ×20/0.95 NA, water immersion (Olympus). An IR-blocking (heat) mirror (Calflex-X;Linos AG) was used as the emission filter in front of the GaAsP photomultipliers (H7422P-40mod; Hamamatsu). The isoflurane-anesthetized mouse (1.5–2.0% in 1 liter O₂/min) was maintained at 36–37°C by a feedback-regulated heating blanket (Letica). Imaging was done through the thinned skull except for the CNQX experiments below. A single whisker was deflected for 1 ms 7° in the anterior–posterior direction. Alternatively, the whole pad was stimulated by 10-ms air puffs. Per stimulus, 1,024 lines at 0.8 ms per line were acquired, and 400 trials were averaged.

For the recording of spontaneous activity the isoflurane concentration was switched between 1.5–2% and 0%. After the EEG showed stable conditions for either the anesthetized state (large oscillations or ''sleep spindles'') or the awake state (small-amplitude fluctuations without transients), 25,600 line scans were acquired rostrocaudally at 2 ms per line and a line length of 256 μm at focus depths of 40, 80, 120, or 160 μm below the pia, starting at alternating depths to avoid sequence-dependent artifacts. At each depth, eight datasets were acquired in the following order: two anesthetized, four awake, and two anesthetized. Images were taken before and after the set of line scans and showed only mild (<20%) bleaching at the line scan position after eight datasets. The EEG was bandpass-filtered (0.1–500 Hz) and also acquired during imaging.

For CNQX experiments, coverslip and agarose were removed, and a 100- to 200-μm-wide opening was made in the dura. The agar and coverslip were replaced before control imaging before removing them again to topically apply 20 μM CNQX, after which 20 min was allowed for penetration into the cortex. The agar and coverslip were restored before imaging resumed. For washout we waited 40 min after imaging with CNQX.

Analysis. Data analysis was performed with MatLab (The MathWorks) and IgorPro (WaveMetrics). Only line scans without movement artifacts, i.e., bumps or spikes in the $\Delta F/F(t)$ traces, were included. For sensory-evoked signals $\Delta F/F(t) = (F(t) - F_0)/F_0$ with F_0 being the average of the 20 pixels before stimulus onset. No bleaching correction was applied. To analyze the temporal dynamics the following α function was fit to the data:

$$f(t) = A \frac{t-d}{\tau} \exp\left(1 - \frac{t-d}{\tau}\right),$$

where A is the amplitude, d the delay (latency), and τ the time constant. In the case of spontaneous activity, the line scan was divided into four segments, each 64 μm long. The values within the segments were averaged, yielding a single time trace

$F_n(t)$, $n = 1, 2, 3, 4$, of 205 s length for each segment. For the spontaneous activity traces, a sliding $F_{n0}(t)$ calculation was used: $F_n(t)$ was boxcar filtered (8-s window), and the resulting $F_{n0}(t)$ was used to calculate $\Delta F/F_n(t) = (F_n(t) - F_{n0}(t))/F_{n0}(t)$. The first and last 4 s of the traces were removed to prevent edge effects. Three CCs of four traces with a center-to-center distance of 64 μm were calculated and averaged. Correlations for segment pairs with the same center-to-center segment distance were averaged. CCs were normalized by the standard deviations of the two correlated traces $\Delta F/F_m$ and $\Delta F/F_n$, and the number of overlapping time points p of the traces at a given Δt:

$$CC_{mn}(\Delta t) = \frac{\sum_t (\Delta F/F)_m(t) \cdot (\Delta F/F)_n(t - \Delta t)}{\mathrm{std}((\Delta F/F)_m(t)) \cdot \mathrm{std}((\Delta F/F)_n(t)) \cdot p}.$$

For the coherence spectra, the complex, normalized cross-spectral densities were calculated pairwise from the segments

$$NCSD_{mn}(f) = \frac{P_{mn}(f)}{\sqrt{P_{mm}(f)P_{nn}(f)}},$$

where P_{mn} is the cross-spectral density and P_{mm} and P_{nn} the power spectral densities. $NCSD_{mn}(f)$ spectra were averaged before calculating the average coherence spectrum. Cross-spectral density was estimated by Welch's averaged, modified periodogram method. For distance-dependence plots (Fig. 3f) the line scan was divided into 16 segments, each 16 μm long.

To check artifacts of the acquisition system, control experiments were done with fluorescein solutions in water (data not shown). They confirmed that sharp lines seen in the power spectra and coherence spectra (at 6.5 and 13.0 Hz) are setup-related artifacts that were routinely removed from all spectra.

To calculate VSD-signal PS and CCs between VSD signals and EEG averages, the complete VSD line scan (256 μm in length, 205-s recording time) was used.

1. Gabbott PL, Somogyi P (1986) Quantitative distribution of GABA-immunoreactive neurons in the visual cortex (area 17) of the cat. *Exp Brain Res* 61:323–331.
2. Larkum ME, Senn W, Luscher HR (2004) Top-down dendritic input increases the gain of layer 5 pyramidal neurons. *Cereb Cortex* 14:1059–1070.
3. Cauller LJ, Clancy B, Connors BW (1998) Backward cortical projections to primary somatosensory cortex in rats extend long horizontal axons in layer I. *J Comp Neurol* 390:297–310.
4. Lubke J, Feldmeyer D (2007) Excitatory signal flow and connectivity in a cortical column. *Brain Struct Funct* 212:3–17.
5. Lu SM, Lin RC (1993) Thalamic afferents of the rat barrel cortex. *Somatosens Mot Res* 10:1–16.
6. Trageser JC, et al. (2006) State-dependent gating of sensory inputs by zona incerta. *J Neurophysiol* 96:1456–1463.
7. Grinvald A, Hildesheim R (2004) VSDI: A new era in functional imaging of cortical dynamics. *Nat Rev Neurosci* 5:874–885.
8. Mitzdorf U (1985) Current source-density method and application in cat cerebral cortex: Investigation of evoked potentials and EEG phenomena. *Physiol Rev* 65:37–100.
9. Brock LG, Coombs JS, Eccles JC (1952) The recording of potentials from motoneurones with an intracellular electrode. *J Physiol* 117:431–460.
10. Matsumura M, Cope T, Fetz EE (1988) Sustained excitatory synaptic input to motor cortex neurons in awake animals revealed by intracellular recording of membrane potentials. *Exp Brain Res* 70:463–469.
11. Waters J, Larkum M, Sakmann B, Helmchen F (2003) Supralinear Ca2+ influx into dendritic tufts of layer 2/3 neocortical pyramidal neurons *in vitro* and *in vivo*. *J Neurosci* 23:8558–8567.
12. Zhu Y, Zhu JJ (2004) Rapid arrival and integration of ascending sensory information in layer 1 nonpyramidal neurons and tuft dendrites of layer 5 pyramidal neurons of the neocortex. *J Neurosci* 24:1272–1279.
13. Nevian T, Larkum ME, Polsky A, Schiller J (2007) Properties of basal dendrites of layer 5 pyramidal neurons. *Nat Neurosci* 10:206–214.
14. Bruno RM, Sakmann B (2006) Cortex is driven by weak but synchronously active thalamocortical synapses. *Science* 312:1622–1627.
15. Lampl I, Reichova I, Ferster D (1999) Synchronous membrane potential fluctuations in neurons of the cat visual cortex. *Neuron* 22:361–374.
16. Denk W, Strickler JH, Webb WW (1990) 2-photon laser scanning fluorescence microscopy. *Science* 248:73–76.
17. Hubener G, Lambacher A, Fromherz P (2003) Anellated hemicyanine dyes with large symmetrical solvatochromism of absorption and fluorescence. *J Phys Chem B* 107:7896–7902.
18. Kuhn B, Fromherz P (2003) Anellated hemicyanine dyes in a neuron membrane. *J Phys Chem B* 107:7903–7913.
19. Kuhn B, Fromherz P, Denk W (2004) High sensitivity of Stark-shift voltage-sensing dyes by one- or two-photon excitation near the red spectral edge. *Biophys J* 87:631–639.
20. Berger T, et al. (2007) Combined voltage and calcium epifluorescence imaging *in vitro* and *in vivo* reveals subthreshold and suprathreshold dynamics of mouse barrel cortex. *J Neurophysiol* 97:3751–3762.
21. Svoboda K, Denk W, Kleinfeld D, Tank DW (1997) *In vivo* dendritic calcium dynamics in neocortical pyramidal neurons. *Nature* 385:161–165.
22. Stosiek C, Garaschuk O, Holthoff K, Konnerth A (2003) *In vivo* two-photon calcium imaging of neuronal networks. *Proc Natl Acad Sci USA* 100:7319–7324.
23. Petersen CCH, Grinvald A, Sakmann B (2003) Spatiotemporal dynamics of sensory responses in layer 2/3 of rat barrel cortex measured in vivo by voltage-sensitive dye imaging combined with whole-cell voltage recordings and neuron reconstructions. *J Neurosci* 23:1298–1309.
24. Kleinfeld D, Delaney KR (1996) Distributed representation of vibrissa movement in the upper layers of somatosensory cortex revealed with voltage-sensitive dyes. *J Comp Neurol* 375:89–108.
25. Brecht M, Roth A, Sakmann B (2003) Dynamic receptive fields of reconstructed pyramidal cells in layers 3 and 2 of rat somatosensory barrel cortex. *J Physiol* 553:243–265.
26. Orbach HS, Cohen LB, Grinvald A (1985) Optical mapping of electrical activity in rat somatosensory and visual cortex. *J Neurosci* 5:1886–1895.
27. Steriade M (2006) Grouping of brain rhythms in corticothalamic systems. *Neuroscience* 137:1087–1106.
28. Mitra PP, Pesaran B (1999) Analysis of dynamic brain imaging data. *Biophys J* 76:691–708.
29. Grinvald A, Manker A, Segal M (1982) Visualization of the spread of electrical activity in rat hippocampal slices by voltage-sensitive optical probes. *J Physiol* 333:269–291.
30. Williams V, Grossman RG, Edmunds SM (1980) Volume and surface area estimates of astrocytes in the sensorimotor cortex of the cat. *Neuroscience* 5:1151–1159.
31. Braitenberg V, Schüz A (1998) *Cortex: Statistics and Geometry of Neuronal Connectivity* (Springer, Berlin).
32. Mokeichev A, et al. (2007) Stochastic emergence of repeating cortical motifs in spontaneous membrane potential fluctuations in vivo. *Neuron* 53:413–425.
33. Herkenham M (1980) Laminar organization of thalamic projections to the rat neocortex. *Science* 207:532–535.
34. Cauller L (1995) Layer I of primary sensory neocortex. *Behav Brain Res* 71:163–170.
35. Cauller LJ, Kulics AT (1988) A comparison of awake and sleeping cortical states by analysis of the somatosensory-evoked response of postcentral area 1 in rhesus monkey. *Exp Brain Res* 72:584–592.
36. Jackson ME, Cauller LJ (1998) Neural activity in SII modifies sensory evoked potentials in SI in awake rats. *Neuroreport* 9:3379–3382.
37. Lysakowski A, Wainer BH, Rye DB, Bruce G, Hersh LB (1986) Cholinergic innervation displays strikingly different laminar preferences in several cortical areas. *Neurosci Lett* 64:102–108.
38. Arbuthnott GW, MacLeod NK, Maxwell DJ, Wright AK (1990) Distribution and synaptic contacts of the cortical terminals arising from neurons in the rat ventromedial thalamic nucleus. *Neuroscience* 38:47–60.
39. Gulledge AT, Kampa BM, Stuart GJ (2005) Synaptic integration in dendritic trees. *J Neurobiol* 64:75–90.
40. Olson CR (2001) Object-based vision and attention in primates. *Curr Opin Neurobiol* 11:171–179.
41. Vogt BA, Pandya DN (1978) Cortico-cortical connections of somatic sensory cortex (areas 3, 1 and 2) in the rhesus monkey. *J Comp Neurol* 177:179–191.
42. Stuart GJ, Palmer LM (2006) Imaging membrane potential in dendrites and axons of single neurons. *Pflügers Arch* 453:403–410.

NEUROSCIENCE

Kuhn et al.